

Whole-process analysis and implementation of a self-powered wireless health monitoring system for railway bridges: Theory, simulation and experiment

Weiqliang Sheng^a, Hongjun Xiang^{a,*}, Linglong Gao^b, Jianjun Wang^c, Junrui Liang^b, Zhiwei Zhang^d

^a School of Civil Engineering, Beijing Jiaotong University, Beijing 100044, China

^b School of Information Science and Technology, ShanghaiTech University, Shanghai 201210, China

^c Department of Applied Mechanics, University of Science and Technology Beijing, Beijing 100083, China

^d Department of Civil Engineering, Beijing Forestry University, Beijing 100083, China

ARTICLE INFO

Keywords:

Wireless health monitoring
Piezoelectric
Railway bridge
Vibration energy harvesting
Internet-of-Things

ABSTRACT

In this work, a self-powered wireless health monitoring system (SP-WHMS) combined with the Internet-of-Things (IoT) is proposed and implemented for a long-term and long-distance health monitoring of railway bridges. This system frees the wireless sensor nodes (WSNs) from their dependence on chemical batteries by using the piezoelectric energy harvester (PEH) to harvest the vibration energy from bridges to power the WSNs. The whole-process of the SP-WHMS including energy conversion, energy storage, energy management and application is analyzed at the first time through theory, simulation and experiment. For the energy conversion, a reported PEH model with high energy conversion efficiency (called D-M PEH) is refabricated, which can achieve a maximum average output power of 0.9 W under unit harmonic acceleration excitation. For the energy storage, a high-precision iteration analysis procedure (IAP) is proposed to predict the charging process of the strong-coupled PEHs and the charging process under non-harmonic excitations. The comparison results show that the IAP's prediction deviates less than 3% from the experiment result and even less than 1% from the simulation result. For the energy management, an AP64500 chip with two adjustable input voltage thresholds and a stable output voltage ensures the normal operation of the SP-WHMS and makes the SP-WHMS suitable for different types of WSNs. For the application, the synergies between energy conversion, storage and management are considered, and the effectiveness of the SP-WHMS used on railway bridges is tested through an activation experiment. This work provides a technical guidance and framework for the implementation of the self-powered wireless monitoring on railway bridges.

1. Introduction

Railway bridges play an important role in the railway system. In some urban rail transit lines of China, bridges even have occupied more than 90% of the total length of the rail line. However, the continually dynamic action of train loads leads to deterioration of bridge health. To ensure the safe operation of the railway system, it is necessary to build a long-term and long-distance health monitoring for railway bridges, so the wireless health monitoring systems (WHMSs) are widely used on railway bridges [1,2]. However, providing a reliable and stable power supply for the wireless sensor nodes (WSNs) is still an engineering challenge. Conventional WSNs used in civil engineering are mainly powered by chemical batteries [3,4] or cables [5]. The chemical batteries have a short lifespan, and replacing the batteries for the WSNs is a laborious and costly task when the bridges are located in remote or hard-to-reach

areas. Powering the WSNs through cables is also undesirable because it reduces the flexibility of the WHMS. Therefore, the concept of self-powered WHMS (SP-WHMS) has been proposed by harvesting vibration energy from bridges to power the WSNs. Although the SP-WHMS has been widely investigated in the civil engineering, there are few reports of its application in railway bridges [6]. In general, the application of bridge vibration energy to power the WSNs involves the following three processes: energy conversion, energy storage and energy management.

Over the past decade, many researchers have investigated different forms of energy transducers to harvest the vibration energy from railway bridges, including electromagnetic transducers [7,8] and piezoelectric transducers [9–11]. Compared to the electromagnetic transducers, the performance of the piezoelectric transducers is better because of their simpler design and higher power density [12]. Therefore, the

* Corresponding author.

E-mail address: hjxiang@bjtu.edu.cn (H. Xiang).

<https://doi.org/10.1016/j.engstruct.2024.118584>

Received 13 December 2023; Received in revised form 3 July 2024; Accepted 5 July 2024

Available online 16 July 2024

0141-0296/© 2024 Elsevier Ltd. All rights are reserved, including those for text and data mining, AI training, and similar technologies.

application of the piezoelectric transducers on railway bridges has received great attention, and many structural types for the piezoelectric transducers have been proposed to improve energy conversion efficiency. Based on the cantilever beam structure, Zhang et al. [13] designed two PEHs with different frequencies to test piezoelectric energy harvesting from bridge vibration on a vehicle–bridge coupling platform. The test results show that when the PEHs are designed to match the natural frequency of bridge or the vibration frequency of vehicle–bridge coupling system, the voltage output is considerable. By combining the cymbal PEH and multilayer stacks, Hou et al. [14] proposed a novel PEH model (PE-VEH) with high bearing capacity and high energy harvesting efficiency for harvesting the vibration energy from the steel-spring floating slab track system on railway bridges. Theoretical predictions and FE simulation results indicate that the total harvested energy would reach up to 31.4 kJ per day when 144 PE-VEHs are arranged on the example bridge. Recently, by incorporating a dynamic amplifier and four cymbal piezoelectric transducer cells (PT-cells), Sheng et al. [15] proposed a dynamic-magnified piezoelectric energy harvester (D-M PEH). Under a real bridge acceleration excitation, the maximum output power of the D-M PEH can reach 0.728 W, which basically meets the power requirement of most commercial WSNs [16]. In addition, many researchers also attempted to harvest other forms of ambient vibration energy using the piezoelectric transducers, such as track vibration [17,18], train vibration [19] and ambient wind energy [20–22]. However, above studies are limited to the energy conversion process, where only the energy harvesting efficiency of the transducers connected to a pure resistor or an open-circuit was investigated, and the harvested energy had not been used to power the WSNs.

Since most commercially available WSNs are powered by direct current (DC), the alternating current (AC) generated by the PEHs subjected to vibrations cannot directly power the WSNs. Therefore, suitable energy storage circuits (ESCs) with rectifiers are needed to convert the AC power into a stable DC power and store the harvested energy. The standard energy harvesting (SEH) circuit [23], consisting of a rectifier bridge and a storage capacitor, is the simplest energy storage circuit. The AC power generated by the PEHs is converted to DC power by the rectifier bridge and the harvested energy is stored in the storage capacitor. Wang et al. [24] proposed a compressive-mode high-power-density PEH and interfaced it with a SEH circuit for harvesting vibration energy from spring suspension systems. A 1 mF storage capacitor was charged to saturation within 18.1 s and 420 low power-dissipation LED diodes were successfully lit. Zhang et al. [25] presented a semi-analytical solution for the charging process of the PEH interfaced with the SEH circuit. This semi-analytical solution is able to accurately predict the charging process under harmonic excitation, but it is not applicable to the case of non-harmonic excitation, such as the train-induced bridge vibration excitation. In addition, many researchers [12,26–28] tried to improve the energy storage efficiency of the PEHs by choosing or designing suitable ESCs, but the energy storage process was mainly focused in their studies, and the stored energy was not used to power the WSNs.

In general, WSNs require a constant and stable supply voltage during activation. However, the voltage on the storage capacitor is not stable and may exceed the operating voltage of the WSNs, so the stored energy needs to be adjusted by the energy management circuit (EMCs) before powering the WSNs. Some commercial chips can be used to design the EMC for energy harvesting. The LTC3588 chip, which can output a stable voltage, is widely used in vibration energy harvesting [24,29–31]. Wang et al. [30] implemented a self-powered temperature monitoring scheme for the train cold chain logistics container by using the LTC3588 chip, where a temperature WSN based on the ZigBee protocol was powered by the PEH. Since the LTC3588 chip has only one voltage threshold, it is not suitable for some WSNs with long activation time or data transmission time. Recently, Wang et al. [32] realized a self-powered wireless temperature sensing system

in the laboratory. In their work, the ViPSN [33,34], whose transmission model is based the Bluetooth low-energy protocol, was powered by the PEH. The WSNs based on the ZigBee or Bluetooth protocol can be easily activated due to the low-power consumption and short data transmission time, but the short transmission distance limits their application on the railway bridges. For the railway bridges, especially those in remote areas, the wireless transmission modes with long transmission distance and strong anti-interference ability are more suitable, such as the LoRa technology. The communication range of the LoRa network can over than ten kilometers in the suburbs [35]. The LoRa Gateway in the LoRa network is used to receive the data from the LoRa Node (i.e., the WSNs) and transmit the data to the cloud server. Once the data is available on the cloud server, it can be received and retrieved worldwide through the IoT platform. However, compared to the WSNs based on the ZigBee or Bluetooth protocol, the WSNs based on the LoRaWAN protocol tend to require higher power consumption and transmission time due to long transmission distance. In addition, for the railway bridges, data that directly reflect the health of the bridge, such as displacements, crack widths and settlements, receive more attention than temperature data.

Although the SP-WHMS for railway bridges has been widely studied in the past two decades, these studies have basically been limited to the energy conversion process or energy storage process, while the whole-process of the SP-WHMS, including energy conversion, energy storage, energy management and application, has not been investigated. Moreover, the IoT platform has not yet been applied to the SP-WHMS for railway bridges. Therefore, the main purpose of this work is to realize an IoT-based SP-WHMS for railway bridges and to investigate whole-process of the SP-WHMS as well as the synergies between various processes. The developed IoT-based SP-WHMS really realizes the autonomous sensing for the data of the railway bridge, including the displacement, crack width and settlement, and can provide a reference for the design of other types of SP-WHMS in railway systems.

2. The proposed SP-WHMS

The working principle of the proposed SP-WHMS for railway bridges is shown in Fig. 1. Frequent passing trains on bridges cause a large amount of vibration energy in bridges. By installing the PEH or piezoelectric transducer at a suitable location of the bridge, such as the bottom of the bridge or the inside of the box girder, the bridge vibration energy can be converted into electrical energy and stored in the storage capacitor of the ESC. An EMC is used to monitor the voltage variation of the storage capacitor and output a stabilized voltage to the WSNs, which are arranged on the bridge to monitor its health. Once the WSN (a wireless node wired to a sensor) is activated, the wireless node sends the bridge data received from the sensor to a nearby wireless gateway, which then transmits the bridge data via the IoT platform to the terminals, such as personal computer (PC) and smart phone.

In the SP-WHMS, the WSN is the only device powered by the PEH. As long as trains pass over the bridge, massive vibration energy flows into the WSN and drives the SP-WHMS to operate, thus realizing a long-term and long-distance health monitoring for the bridges. Since the train load is intermittent, when the harvested energy after the train runs one time on the bridge is not enough to activate the WSN, it must to store the harvested energy each time the train runs on the bridge in the storage capacitor. Once the EMC monitors that the energy stored in the storage capacitor meets the activation energy of the WSN, the storage capacitor discharges and the EMC outputs a stable voltage to the WSN. The EMC requires at least two voltage thresholds to ensure that the storage capacitor can continuously discharge during the activation of the WSN.

The whole-process of the SP-WHMS can be divided into the following four parts: energy conversion, energy storage, energy management and application.

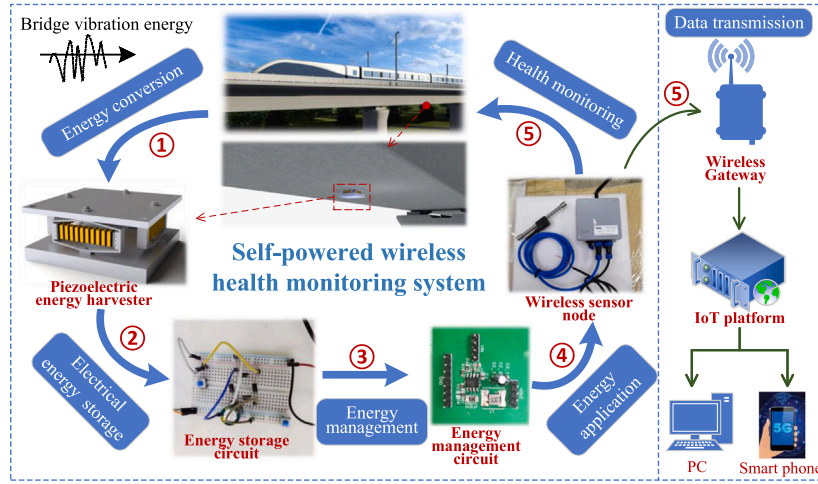


Fig. 1. Working principle of the proposed SP-WHMS for railway bridges.

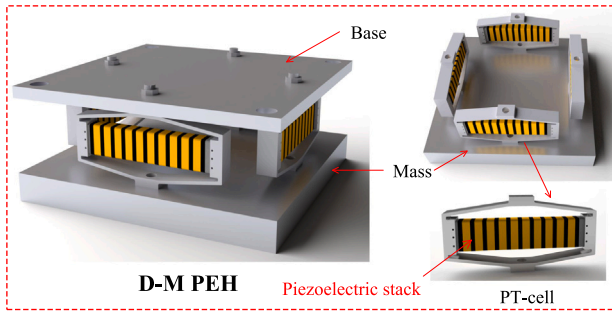


Fig. 2. Structure diagram of the fabricated D-M PEH [15].

3. Energy conversion

3.1. The energy transducer

The first process of the SP-WHMS is to convert the vibration energy of railway bridges into electrical energy, so an energy transducer with high energy conversion efficiency is required for this process. In our previous work [15], a high-efficiency piezoelectric transducer (called D-M PEH), which consists of four piezoelectric transducer cells (PT-cells) and a dynamic amplifier, is proposed for bridge vibration energy harvesting, as shown in Fig. 2. The results show that when a train passes through the bridge, the maximum output power and harvested energy reach 728 mW and 664 mJ, respectively, which are sufficient to meet requirements of most commercial WSNs. However, such a high output power of the D-M PEH is obtained under the pure resistance circuit (i.e., the D-M PEH is connected to a pure resistor), as shown in Fig. 3. The harvested energy is dissipated by the pure resistance in the form of thermal energy, but not stored and used to power the WSNs.

3.2. Parameter determination

Since the fabricated D-M PEH model in the previous work was damaged, we refabricate a D-M PEH model with the same dimensions in this work, and use it as the energy transducer for the SP-WHMS. The geometric parameters and the material parameters of the refabricated D-M PEH can be found in Ref. [15]. It should be noted that the electrical parameters of the piezoelectric stack (i.e., the dielectric permittivity at constant stress ϵ_{33}^T and the piezoelectric strain constant d_{33}) produced in different batches may vary slightly due to the processing differences. Moreover, the preloading applied to the piezoelectric stack for a long

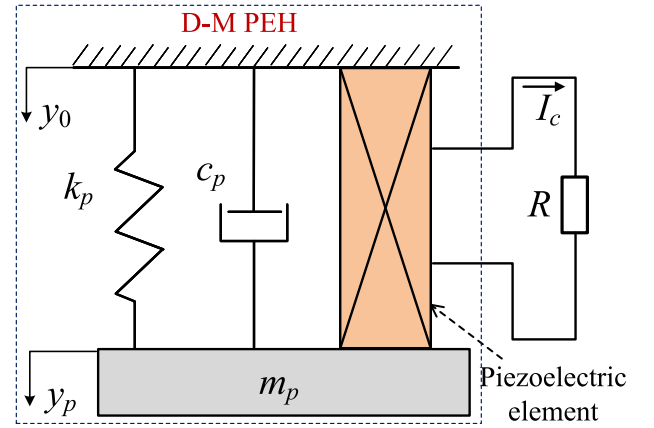


Fig. 3. Schematics of the D-M PEH interfaced with a pure resistor.

time may reduce the piezoelectric strain constant d_{33} . Therefore, the ϵ_{33}^T and d_{33} of the refabricated D-M PEH model in this work need to be determined first for further theoretical analysis. An effective method to determine these two electrical parameters (ϵ_{33}^T and d_{33}) is as follows: firstly, measure the voltage–frequency response of the D-M PEH at a certain resistance and the power–resistance relationship of the D-M PEH under a resonant excitation through experiment, respectively; Then to obtain the voltage–frequency curve and the power–resistance curve of the D-M PEH through theoretical analysis; Finally, to adjust the theoretical curves by changing ϵ_{33}^T and d_{33} , and then the ϵ_{33}^T and d_{33} of the refabricated D-M PEH can be determined when the theoretical curves are matched the experiment results. The following is the detailed process for determining ϵ_{33}^T and d_{33} .

The D-M PEH can be considered as a single-degree-of-freedom (SDOF) system consisting of a mass block, a spring, a damper and the piezoelectric element, which is the same as the simplified model of some typical resonant PEHs [23,36,37], as shown in Fig. 3. The electromechanical coupling equation of the D-M PEH under base vibration excitation can be written as follows:

$$\mathbf{M}\ddot{\mathbf{X}} + \mathbf{C}\dot{\mathbf{X}} + \mathbf{K}\mathbf{X} = \mathbf{P} \quad (1)$$

where

$$\mathbf{M} = \begin{bmatrix} m_p & 0 \\ 0 & 0 \end{bmatrix}, \quad \mathbf{C} = \begin{bmatrix} c_p & 0 \\ \theta_p & -C_p \end{bmatrix}, \quad \mathbf{K} = \begin{bmatrix} k_p & \theta_p \\ 0 & 0 \end{bmatrix},$$

$$\mathbf{X} = \begin{bmatrix} y_p(t) \\ V_p(t) \end{bmatrix}, \quad \mathbf{P} = \begin{bmatrix} F(t) \\ I_c(t) \end{bmatrix}$$

Table 1
The lumped parameters of the refabricated D-M PEH.

Parameters	m_p	k_p	θ_p	C_p	ξ_p
Value	5.420 kg	1.560×10^5 N/m	1.428×10^{-2} N/V	67.560 nF	0.22%

where V_p is the output voltage of the D-M PEH; $F(t) = -m_p \ddot{y}_0$ is the excitation force; m_p is the mass of the mass block, and in this work, $m_p = 5.420$ kg; y_0 is the displacement of the base; y_p is the relative displacement between the mass and base; $c_p = 2m_p \omega_p \xi_p$ is the mechanical damping, where ω_p and ξ_p are the natural frequency and damping ratio of the short-circuit D-M PEH, respectively, which can be obtained from its acceleration time history and frequency spectrum under an impact load [15]. Here, we get $\omega_p = 2\pi \times 27$ rad/s = 169.6 rad/s and $\xi_p = 0.22\%$; k_p is the equivalent stiffness of the D-M PEH and can be calculated by $k_p = m_p \omega_p^2 = 1.560 \times 10^5$ N/m; θ_p and C_p are the equivalent coupling coefficient and equivalent capacitance of the D-M PEH, which are the functions of ε_{33}^T and d_{33} , and can be calculated according to the theoretical formulas given in Ref. [15]. Once the other parameters of the D-M PEH are determined, θ_p and C_p are determined by ε_{33}^T and d_{33} only. I_c is the output current across the electrodes of the piezoelectric element; When the D-M PEH is connected to a pure resistor R (see Fig. 3), $I_c = V_p/R$.

Since the pure resistor is a linear element, there is a linear relationship between the input (acceleration and displacement of the base) and output (y_p and V_p) of the D-M PEH. For the case of the D-M PEH is interfaced to a pure resistance circuit, the voltage output and power output frequency response functions can be written as follows [15]:

$$V_{p0} = \frac{\theta_p R m_p \omega_0 A_0}{\sqrt{[k_p - (m_p + R C_p c_p) \omega_0^2]^2 + [(R C_p k_p + R \theta_p^2 + c_p) \omega_0 - m_p R C_p \omega_0^3]^2}} \quad (2)$$

$$P_{out} = \frac{1}{2R} \frac{(\theta_p R m_p \omega_0 A_0)^2}{[k_p - (m_p + R C_p c_p) \omega_0^2]^2 + [(R C_p k_p + R \theta_p^2 + c_p) \omega_0 - m_p R C_p \omega_0^3]^2} \quad (3)$$

where V_{p0} is the amplitude of V_p , and P_{out} denotes the average output power of the D-M PEH; A_0 and ω_0 denote the acceleration amplitude and frequency of the base, respectively.

The experimentally measured voltage–frequency responses and power–resistance relationship of the D-M PEH under harmonic acceleration excitations with an amplitude of 1 m/s^2 are shown in Fig. 4. The layout of the experiment setup is the same as that of the charging experiment in Section 4, except that the SEH circuit is replaced by a pure resistor. When $\varepsilon_{33}^T = 40.73$ nF/m and $d_{33} = 320 \times 10^{-12}$ C/N, the theoretical curves and the experiment results are almost identical, as shown in Fig. 4. Therefore, the parameters ε_{33}^T and d_{33} of the piezoelectric material in the refabricated D-M PEH are approximately equal to 40.73 nF/m and 320×10^{-12} C/N, respectively. As a result, the equivalent coupling coefficient θ_p and equivalent capacitance C_p of the D-M PEH are calculated to be 1.428×10^{-2} N/V and 67.560 nF, respectively. The lumped parameters of the refabricated D-M PEH are listed in Table 1. In addition, it can be seen from Fig. 4(b) that the maximum average output power of the fabricated D-M PEH can reach 0.9 W, such a high output power is very considerable for vibration energy harvesting in railway bridge.

4. Energy storage

4.1. Energy storage circuit (ESC)

When the D-M PEH is subjected to bridge vibration excitation, alternating current (AC) is generated on the piezoelectric material, but most

WSNs in many applications require a stable direct current (DC) power supply. Therefore, suitable ESCs with a rectifier are needed to convert the AC power into DC power and store the harvested energy, such as the following four typical ESCs: SEH circuit [38], SCE circuit [39], P-SSHI circuit [37,40] and S-SSHI circuit [41,42]. Under a certain excitation, the energy storage efficiency of these four typical ESCs is related to the coupling condition of the PEH, which can be determined according to the value of the discriminant coefficient $\eta = \kappa^2 - 4\xi_p^2 - 4\xi_p$, where $\kappa^2 = \theta_p^2 / (C_p k_p)$ is the dimensionless electro-mechanical coupling constant. For weak coupling, $\eta < 0$; for critical coupling, $\eta = 0$; and for strong coupling, $\eta > 0$ [43]. For the fabricated D-M PEH in this work, $\kappa^2 = 0.0193$ and $\eta = 0.01 > 0$, so it can be determined that the refabricated D-M PEH is strongly coupled. For a PEH with strong coupling condition, the SEH and S-SSHI circuits are more efficient as compared to the other two circuits [25]. In S-SSHI circuit, a part of the energy generated by the PEH is lost by the synchronized switch and inductor, and the complexity of the synchronized switch makes it difficult to manufacture. Compared to the S-SSHI circuit, the SEH circuit, which consists of only a bridge rectifier and a storage capacitor, is much simpler in structure and has almost no energy loss except for a very small portion of the energy lost by the diode. Therefore, in this work, the SEH circuit is selected as the ESC for the SP-WHMS.

As mentioned above, in Ref. [15], the high output power of the D-M PEH was measured in the pure resistance circuit. However, it is not clear whether such high energy conversion efficiency can still be maintained when the D-M PEH is connected to a SEH circuit, so the next work aims to achieve the maximum energy conversion efficiency (or energy storage efficiency) for the D-M PEH with a SEH circuit by selecting appropriate parameters.

4.2. Theoretical analysis of the charging process

Fig. 5 shows the D-M PEH connected to the SEH circuit, which consists of a storage capacitor C_r and a full-bridge rectifier composed of four diodes. The voltage across C_r and the forward voltage drop in each diode are V_r and V_d , respectively.

For the case of the D-M PEH is interfaced to the SEH circuit, Fig. 6 shows the waveforms of V_p , V_c and i_c during charging, where $V_c = V_r + 2V_d$. i_c denotes the charging current of C_r and is equal to the absolute value of I_c , i.e., $i_c = |I_c|$. When the absolute value of the voltage across the piezoelectric element $|V_p|$ is less than V_c , the circuit is blocked and there is no current (i.e., $i_c = 0$). Once $|V_p|$ increases to $|V_c|$, the circuit is conducted and C_r is charged. θ_1 and θ_2 in Fig. 6 denote the block angles of the rectifier in one cycle.

The presence of a nonlinear bridge rectifier in the SEH circuit causes the output and input of the system to no longer maintain a linear relationship, which makes it difficult to obtain analytical expressions for the output results, including V_r and I_c , during the charging process. Therefore, this part presents a numerical iteration method to predict the charging process of the system that a D-M PEH interfaced with the SEH circuit under arbitrary excitation.

The iteration analysis procedure (IAP) is shown in Fig. 7, and can be divided into four steps as follows:

- (1) Set the initial motion of the D-M PEH, the voltage V_r and V_p , and the current I_c to 0. Determine V_d and the terminal time, and set a small enough iterative time step Δt to ensure accuracy of the iterative process.
- (2) Compare the values of $V_p(t)$ and $V_c(t)$ in the current iteration step, and calculate $I_c(t)$ by

$$I_c(t) = \begin{cases} 0, & |V_p(t)| < V_c(t) \\ \frac{\theta_p \dot{y}_p(t) C_r}{C_r + C_p}, & |V_p(t)| \geq V_c(t) \end{cases} \quad (4)$$

Then, calculate the voltage variation, $\Delta V_r(t)$, on C_r by

$$\Delta V_r(t) = \frac{|I_c(t)| \Delta t}{C_r} \quad (5)$$

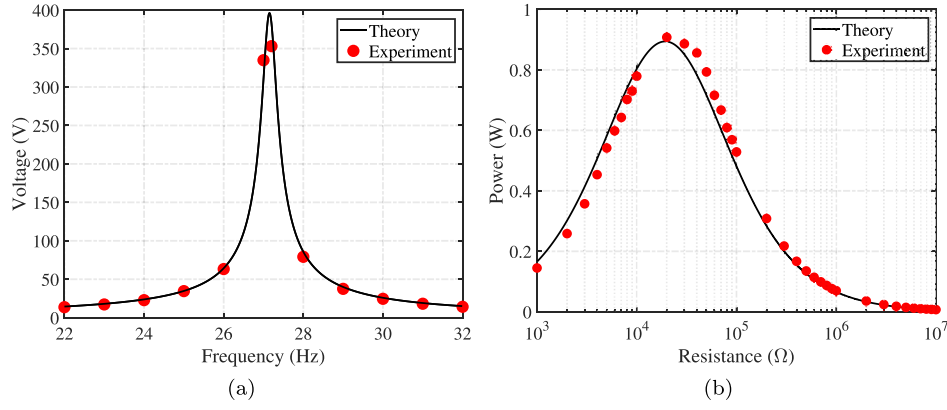


Fig. 4. (a) Voltage–frequency responses of the D-M PEH connected to a resistance $R = 100$ kΩ; (b) Average output power of the D-M PEH versus load resistance under a harmonic acceleration excitation with unit amplitude and frequency of 27 Hz.

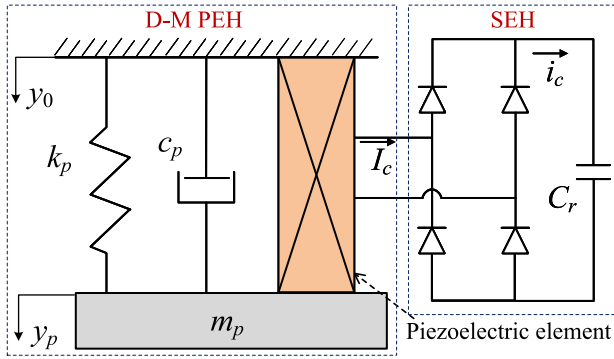


Fig. 5. Schematics of the D-M PEH interfaced with a SEH circuit.

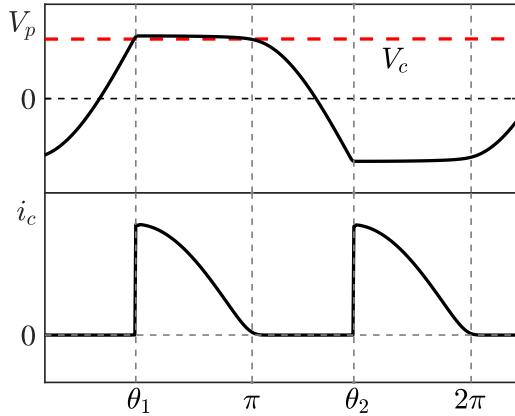


Fig. 6. Schematic of the voltage across the PEH and current flow into the storage capacitor for the SEH circuit.

Before the next iteration, the value of $V_p(t)$ needs to be modified as follows: if $V_p(t) \geq V_c(t)$, then $V_p(t) = V_c(t)$; if $V_p(t) \leq -V_c(t)$, then $V_p(t) = -V_c(t)$.

- (3) Use the motion of the D-M PEH and $V_p(t)$ in the current iteration step as the initial conditions, and then solve the coupling equation (Eq. (1)) by using the Newmark- β algorithm to obtain the motion state and $V_p(t + \Delta t)$ in the next iteration step. Meanwhile, calculate the V_c for the next iteration step by $V_c(t + \Delta t) = V_c(t) + \Delta V_c(t)$.
- (4) Determine whether the interactive terminal time is reached: if not, repeat Step (2) and Step (3); if yes, terminate the iteration.

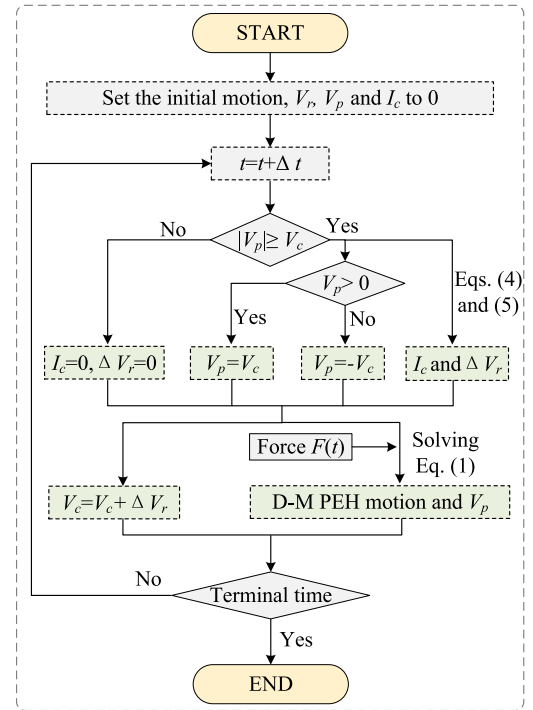


Fig. 7. The IAP of the charging process.

In fact, for the charging process of a PEH interfaced with the SEH circuit, a semi-theoretical solution that can significantly improve the efficiency of the iterative process was given by Zhang et al. [25]. However, compared to the IAP proposed in this work, this semi-analytical solution has some limitations: (1) The excitation must be harmonic. The semi-analytic solution is obtained under harmonic excitation, so it is not applicable when the excitation is non-harmonic, such as the vehicle-induced bridge vibrations. (2) Not suitable for the PEH with high degree of electromechanical coupling. Not only in the work of Zhang et al. [25] but also in many theoretical studies on the PEH interfaced with charging interface circuits [41,44,45], there is an assumption that the displacement response of the PEH under a harmonic excitation is also harmonic. According to Eq. (1), the inverse piezoelectric effect of the piezoelectric element produces a reaction force, $F_p = -\theta_p V_p$, between the mass block of the PEH and the base. As mentioned above, when a PEH interfaced with the SEH circuit is subjected to a harmonic force $F(t)$, the output voltage V_p is not harmonic (see Fig. 6), which leads to F_p also being non-harmonic and further leads to the

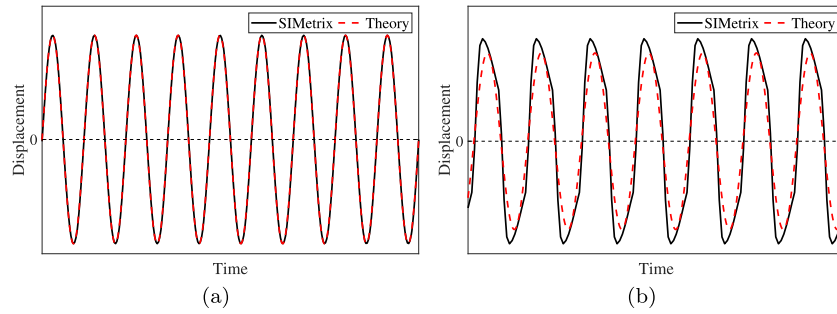


Fig. 8. The steady-state displacement response of the PEH interfaced with the SEH circuit under a harmonic acceleration excitation. (a) weak coupling; (b) strong coupling.

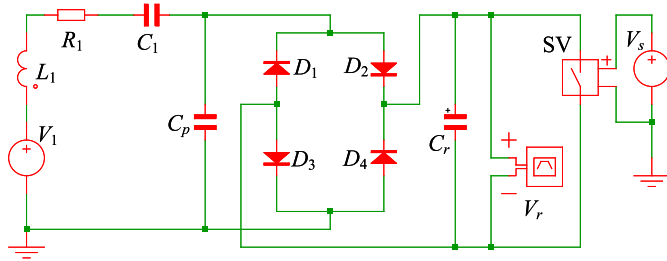


Fig. 9. Equivalent circuit of the D-M PEH with the SEH circuit established in the electronic simulator, SIMetrix.

displacement response of the PEH being non-harmonic. The weight of the non-harmonic component in the displacement response depends on the ratio of F_p to the excitation $F(t)$. Fig. 8 shows the steady-state displacement responses of the PEHs with different coupling degrees under a harmonic excitation when the PEHs are interfaced with the SEH circuit, where the theoretical results are given by the Ref. [23], and the simulation results are obtained using the electronic simulator, SIMetrix. For a PEH with weak electromechanical coupling, F_p is almost negligible with respect to the harmonic force $F(t)$, so the displacement response of the PEH approximates a harmonic curve, as shown in Fig. 8(a). However, as the degree of coupling strengthens, F_p gradually increases so that the displacement response of the PEH becomes non-harmonic, see the simulated curve in Fig. 8(b). (3) No transient response. Since the semi-analytical solution is obtained under steady-state conditions, it results in the transient response being neglected, which leads to large error between theoretical and real results when the transient response is difficult to decay, such as the vibration of the PEH with very low inherent damping. However, the proposed IAP does not have the above limitations.

It should be pointed out that although the semi-analytical solution proposed by Zhang et al. [25] has the above limitations, it is well suited for most resonance-type PEHs subjected to harmonic excitations.

4.3. Simulation and experiment validation

In this part, the electronic simulator SIMetrix is used and a verification experiment is performed to verify the correctness of the proposed IAP.

Based on the analogy between electrical and mechanical domains, the equivalent circuit parameters of the D-M PEH can be determined using the following relations [45,46]:

$$V_1 = \frac{F}{\theta_p}, \quad L_1 = \frac{m_p}{\theta_p^2}, \quad R_1 = \frac{c_p}{\theta_p^2}, \quad C_1 = \frac{\theta_p^2}{k_p} \quad (6)$$

where V_1 , L_1 , R_1 and C_1 are the equivalent voltage source, equivalent inductance, equivalent resistance and equivalent capacitance, respectively. Fig. 9 shows the D-M PEH with the SEH circuit established in

the SIMetrix. In order to consider only the effect of coupling strength, a voltage control switch SV is used in the circuit to ensure that the charging process starts when the D-M PEH is in steady-state vibration. The switch remains closed for the first 20 s, so the storage capacitor C_r is short-circuited and cannot be charged. Once the switch is opened, the D-M PEH starts charging the storage capacitor. The forward voltage drop in each diode $V_d = 0.5$ V, and $C_r = 100$ μ F. The parameters for the D-M PEH are listed in Table 1, where the damping ratio ξ_p is adjusted to 1% to accelerate the decay of transient response. Three D-M PEHs with different equivalent coupling coefficients θ_p , $2\theta_p$ and $5\theta_p$ are considered, and the corresponding η are -0.0211 , 0.037 and 0.443 , respectively. The larger the value of η , the stronger the coupling. Under a harmonic acceleration excitation with frequency of 27 Hz and amplitude of 0.5 m/s^2 , the variation curves of the voltage across the storage capacitor C_r during the charging process for these three D-M PEHs are shown in Fig. 10. For the D-M PEH with weak coupling (see Fig. 10(a)), the theoretical result calculated with the semi-analytical solution proposed by Zhang et al. [25] agree almost exactly with the simulation result of the SIMetrix. However, as the degree of electromechanical coupling increases, the harmonic assumption for the PEH's displacement leads to an increase in the error between the theoretical and simulation results, see the theoretical results of Zhang et al. and simulated results in Figs. 10(b) and 10(c). Significantly, the IAP's results always agree well with the simulation results (the error less than 1%) regardless of the degree of electromechanical coupling, which proves the reliability of the IAP in predicting the charging process of the PEHs with different coupling conditions.

Next, an experiment was implemented to verify the IAP, and the experiment setup is shown in Fig. 11. A steel base is fixed to four support bars through eight springs, and a D-M PEH model is fixed under the steel base. The vibration signal is controlled and generated by a vibration controller (Keysight 33600 A), and then amplified by a signal amplifier (GF-200 W) to activate the vibration shaker (WS-Z30-50). The force generated by the shaker is transmitted to the steel base through four symmetrically arranged force-transmitting poles, which causes the steel base to vibrate, and further vibrates the D-M PEH. An acceleration sensor (KSI-108A010, single-axis) is mounted at the center of the top of the steel base to monitor the acceleration of the base, and a voltage sensor (DSI-V-200) connected in parallel with the charging capacitor to monitor its voltage changes. The acceleration and voltage data is stored in the computer through a data acquisition instrument (DEWE-43 A, eight channels). The data sampling rate is 2000 Hz, i.e., sampling 2000 data points per second. The frequency resolution is less than 0.02 Hz.

Under a harmonic acceleration excitation with frequency $f_0 = 27$ Hz and amplitude $A_0 = 0.1 m/s^2$, the variations of voltages across storage capacitor C_r during the charging process from experiment, circuit simulation and IAP are shown in Fig. 12. The IAP results are obtained in MATLAB, and the Newmark- β method is adopted in the iteration, with $\beta = 0.25$ and $\gamma = 0.5$; The equivalent circuit parameters of the D-M PEH can be calculated by using Eq. (6), and the results are listed in Table 2. Six storage capacitors with capacitances of 0.1 mF, 0.47 mF, 1 mF, 2.2 mF, 3.3 mF and 4.7 mF, respectively, are tested. As seen in Fig. 12, the

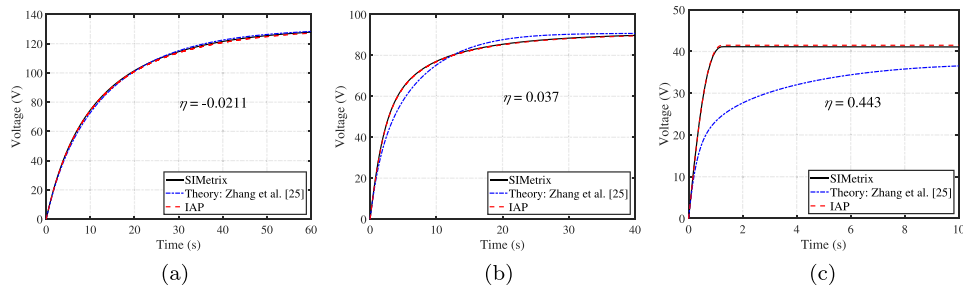


Fig. 10. Variation curves of the voltage across the storage capacitor C_r during the charging process. ($C_r = 100 \mu\text{F}$).

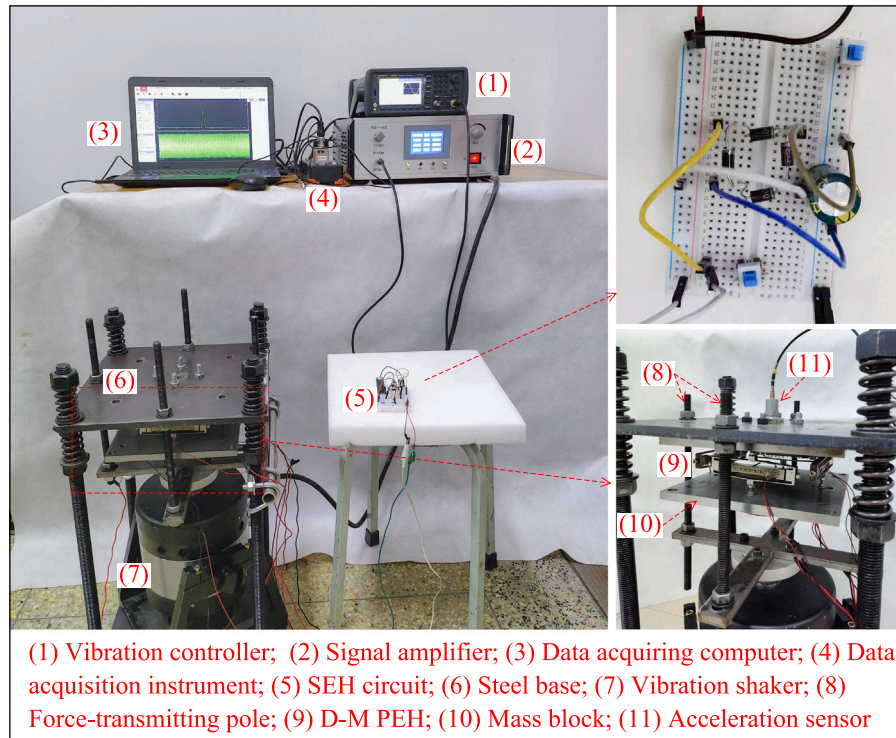


Fig. 11. Experiment setup.

Table 2

Parameters of the equivalent circuit.

Parameters	Value
Amplitude of V_1	37.97 V
Equivalent inductance, L_1	2.67×10^4 H
Equivalent capacitance, C_1	1.31 nF
Equivalent resistance, R_1	19.85 k Ω
Diode forward voltage drop, V_d	0.50 V

IAP results are in good agreement with the experiment and simulation results. For the case of $C_r = 4.7$ mF (Fig. 12(f)), the maximum error between the experiment and IAP results is less than 3%. Significantly, the errors between the simulation and IAP results are less than 1% in all cases.

4.4. Optimal design of the charging process

When a train passes through the bridge, the total energy stored in the storage capacitor during this period is of most interest. The stored energy, E_s , can be calculated by:

$$E_s = \frac{1}{2} C_r (V_r^2 - V_s^2) \quad (7)$$

where V_s and V_r are the voltages across C_r at the start moment t_s and the end moment t_e of charging process, respectively. This part aims to maximize charging efficiency of the D-M PEH interfaced with the SEH circuit by optimizing the charging process. The lumped parameters for the D-M PEH are listed in Table 1.

Fig. 13 shows variations of the stored energy on the storage capacitors in Fig. 12, where the charging start moment $t_s = 0$. The charging efficiency of the storage capacitor varies continuously with the charging duration, and the storage capacitor with the highest charging efficiency varies in different charging time periods. For example, after 5 s of charging duration, the capacitor of 0.1 mF has the largest stored energy of 61.3 mJ; however, after 30 s of charging duration, the total energy stored in the capacitor of 100 μF is the least, while the capacitor of 1 mF exhibits the highest charging efficiency with the largest stored energy of 210.9 mJ.

Under a certain base acceleration excitation, the resonant frequency of the D-M PEH is another significant factor affecting the charging efficiency. For the fabricated D-M PEH in this work, the short-circuit and open-circuit natural frequencies of the D-M PEH are 27.00 Hz and 27.26 Hz, respectively. During charging, the resonant frequency of the D-M PEH will change from 27.00 Hz to 27.26 Hz as the voltage across C_r increases.

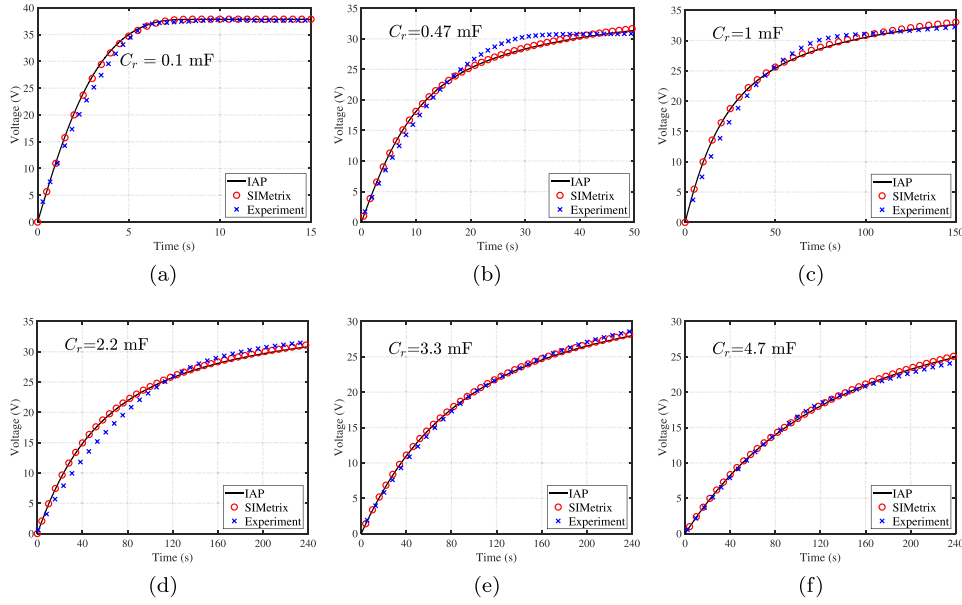


Fig. 12. Variations of voltages across different storage capacitors during the charging process. ($A_0 = 0.1 \text{ m/s}^2$ and $f_0 = 27 \text{ Hz}$).

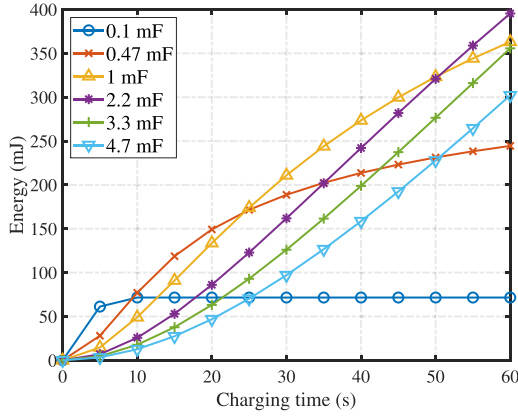


Fig. 13. Variations of the stored energy on different charging capacitors during the charging process. ($A_0 = 0.1 \text{ m/s}^2$ and $f_0 = 27 \text{ Hz}$).

Fig. 14 shows the effect of storage capacitor C_r and excitation frequency f_0 on the stored energy of C_r after different charging durations. The corresponding value in the nephogram is the energy stored in C_r which is calculated by Eq. (7), where both the charging start moment t_s and voltage V_s are 0, so the charging duration $t_c = t_e$. The excitation is a harmonic base acceleration excitation, and its amplitude is the same as the maximum peak acceleration (0.359 m/s^2) in the acceleration spectrum of a railway bridge under a passing train, as shown in Fig. 15. Two peaks appear in the nephograms with different charging durations, and the corresponding excitation frequencies, capacitance of C_r and stored energy are marked in the nephograms, as shown in Fig. 14. As the charging duration increases, the excitation frequencies corresponding to the two peaks remain constant at 27.066 Hz (near the short-circuit natural frequency) and 27.202 Hz (near the open-circuit natural frequency). At the second peak (corresponding to 27.202 Hz), the energy is extremely sensitive to the capacitance of C_r , whereas at the first peak (corresponding to 27.066 Hz), the energy has a very strong robustness to the capacitance of C_r . Moreover, the capacitance of C_r corresponding to the second peak ($C_{r,2}$) is much smaller than that corresponding to the first peak ($C_{r,1}$), and the energies corresponding to the two peaks are very close, with a deviation of less than 5%, so according to Eq. (7), the voltage variation on $C_{r,2}$ is much larger than

that on $C_{r,1}$. For example, when $t_c = 60 \text{ s}$, the voltage variation on $C_{r,2}$ is 326 V, but on $C_{r,1}$ is only 110 V. In general, excessive voltage or voltage fluctuation tends to damage energy management circuits and wireless nodes; in contrast, a stable voltage is easier to manage. Therefore, discussing the first peak is more meaningful for energy storage and management. In the next work, only the first peak is discussed and the parameter corresponding to the first peak is considered as the optimal parameter.

When the initial voltage on C_r is 0, i.e., $V_s = 0$, the variations of the optimal capacitance ($C_{r,opt}$) of C_r and the maximum stored energy ($E_{s,max}$, corresponding to the first peak in Fig. 14) are shown in Figs. 16(a) and 16(b) (the lines with $V_s = 0$), respectively. The voltage variation ΔV on the optimal C_r under a certain charging duration can be calculated by $\Delta V_r = \sqrt{2E_{s,max}C_{r,opt}}$, and the results are shown in Fig. 16(c), where $\Delta V = V_r - V_s$. The ordinate of Fig. 16(c) refers to the voltage variation on the corresponding optimal C_r for the charging duration corresponding to the abscissa of Fig. 16(c). For example, for the line with $V_s = 0$, the optimal capacitance $C_{r,opt}$ is 941 μF for the 60 s charging duration (as shown in Fig. 16(a)), and the ordinate value at the abscissa of 60 s in Fig. 16(c) indicates the voltage variation of the 941 μF C_r after 60 s charging duration. As seen in Fig. 16, for $V_s = 0$, the optimal capacitance $C_{r,opt}$ and the corresponding maximum stored energy increase almost linearly as the charging duration increases, however, the voltage variation on the optimal C_r remains almost constant at 110 V. This means that for different charging capacitors with an initial voltage of 0 V, after a certain charging duration, the capacitor whose voltage just rises to 110 V stores the maximum energy, and its capacitance is the optimal capacitance for that charging duration. Therefore, the charging efficiency of the D-M PEH can be maximized by selecting the optimal storage capacitor based on the charging duration, but the excessive voltage variation (110 V) on the optimal charging capacitor is detrimental to the energy management circuits and WSNs, and the voltage (110 V) on the optimal capacitor at the end of charging process is far exceeds the operating voltage ranges of most tiny energy management circuits and WSNs. An effective way to reduce the voltage and voltage variation on the optimal storage capacitor is to increase the initial voltage V_s across C_r at the charging start moment.

Fig. 16 compares the variations of the optimal capacitance of C_r (Fig. 16(a)), the maximum stored energy (Fig. 16(b)) and the voltage variation ΔV on the optimal C_r (Fig. 16(c)) with the charging duration for different initial voltage V_s . As seen in Fig. 16(c), for a certain

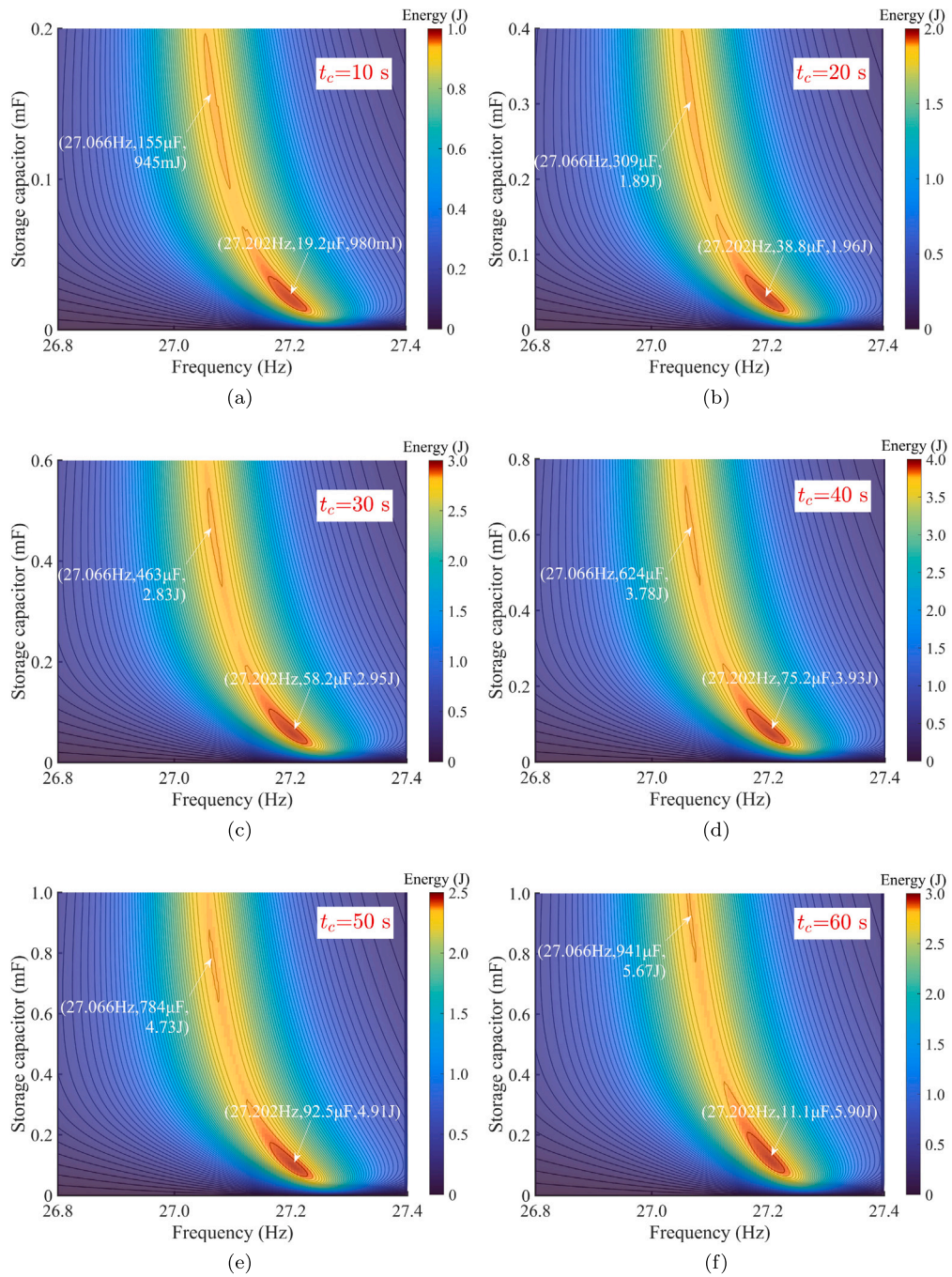


Fig. 14. Effect of capacitance of C_r and excitation frequency on the stored energy after different charging duration t_c . ($A_0 = 0.359 \text{ m/s}^2$).

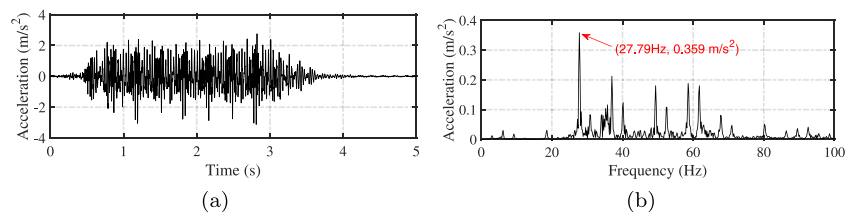


Fig. 15. (a) Quarter-span acceleration response and (b) corresponding frequency spectrum of a Hada high-speed railway bridge under passing train.

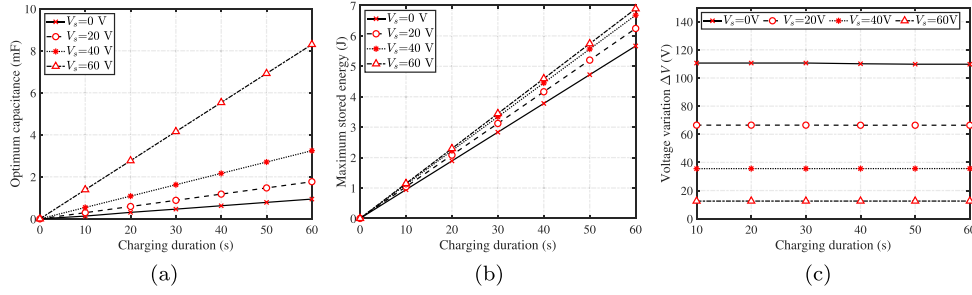


Fig. 16. Variations of (a) the optimal capacitance of C_r , (b) the maximum stored energy, and (c) voltage variation ΔV on the optimal C_r with the charging duration. (V_i : initial voltage across C_r at the charging start moment).

charging duration, both the voltage variation ΔV and final voltage V_r on the optimal charging capacitor decrease as the initial voltage V_s increases. Moreover, the voltage variation ΔV almost unchanged for different charging durations.

As seen in Figs. 16(a) and 16(b), the optimal capacitance and the maximum stored energy of C_r increase linearly with charging duration for different initial voltages. This means that if the optimal capacitance and the maximum stored energy of C_r under a certain charging duration are known, the optimal capacitance and the maximum stored energy of C_r under different charging durations can be predicted by using the linear relationship. At a certain charging duration, the optimal capacitance of C_r increases as the initial voltage of C_r rises, and so does the increase rate. The effect of the initial voltage of C_r on the maximum average charging power of the D-M PEH, P_{\max} , (i.e. the increase rate of the maximum stored energy of C_r with charging duration) is shown in Fig. 17(a), where P_{\max} is obtained by dividing the maximum stored energy on C_r at 60 s charging duration by 60 s. The red dashed line in Fig. 17(a) represents the average power limit (P_{\lim}) of the D-M PEH connected to a pure resistor. P_{\lim} and the corresponding circuit voltage amplitude V_{\lim} can be calculated by [43]:

$$P_{\lim} = \frac{m_p A_0^2}{16 \xi_p \omega_p}, \quad V_{\lim} = \sqrt{2R_{\text{opt}} P_{\lim}} \quad (8)$$

where $\omega_p = \sqrt{k_p/m_p}$; R_{opt} is the corresponding circuit resistor when the average output power reaches P_{\lim} , and its expression is shown in Appendix, here, $R_{\text{opt}} = 21.0$ k Ω . Substituting the parameters of Table 1 and $A_0 = 0.359$ m/s² into Eq. (8) yields $P_{\lim} = 117$ mW and $V_{\lim} = 70.1$ V. As seen in Fig. 17(a), as the initial voltage V_s increases, the maximum average charging power P_{\max} first gradually increases and reaches a peak when V_s rises to V_{\lim} , and then decreases as V_s rises further. The peak value of P_{\max} is 115 mW, reaching 98.29% of P_{\lim} . Due to the presence of the forward voltage drop of the diodes in the SEH circuit, the peak value of the P_{\max} curve is slightly less than P_{\lim} . The voltage variation of the optimal C_r decreases as the initial voltage V_s and is almost equal to 0 as V_s rises near V_{\lim} , as shown in Fig. 17(b). Moreover, the resonant frequency of the D-M PEH (the excitation frequency corresponding to the first peak of the energy nephogram) is almost constant at 27.06 Hz when the initial voltage across C_r rises from 0 to V_{\lim} , as shown in Fig. 17(c).

Fig. 18 shows the energy stored in C_r with different initial voltage under different capacitances of C_r and excitation frequency after one minute of charging durations. As the initial voltage V_s increases, the stored energy is gradually concentrated at the excitation frequency (27.06 Hz) corresponding to the first peak, and the increase in V_s enhances the robustness of the stored energy to the capacitance of C_r . This means that in order to store more energy in a given charging duration using the D-M PEH, a charging capacitor with initial voltage has a larger selectable capacitance range than a charging capacitor without initial voltage. Generally, when the initial voltage is less than the V_{\lim} , the larger the initial voltage, the larger the selectable capacitance range.

5. Energy management and application

5.1. Power supply demand

In existing studies of piezoelectric SP-WHMS, low-power temperature WSNs or LED diodes are usually used as the powered devices [24, 30,32]. For railway bridges, however, indicators that directly reflect structural safety are more worthy of being monitored, such as bridge displacement and crack width.

In this study, a commercial displacement WSN, ZRQ-L2018, produced by the Beijing Zhiruquan Technology Co., Ltd is the only device in the displacement wireless sensing system powered by the D-M PEH, as shown in Fig. 19. In the displacement WSN, the displacement sensor is wired to the displacement wireless node, and can be used to monitor the displacement, settlement, slip and crack width of bridges [47–49]. The displacement WSN has a wide DC working voltage of 8–12 V, and the wireless module utilizes the high-efficiency ISM-band RF Lora spread spectrum chip, with the standby current of 10 μ A, a transmitting current of 100 mA, a receiving current of 12 mA, and a maximum transmission distance of 5 km in an open field. The energy required to activate the displacement WSN once is about 2 J. The WSN transmits the data received from the sensor at regular intervals to the wireless gateway, which then sends the data to the PC via the IoT platform. The time interval for data transmission can be adjusted arbitrarily and is 60 s in this work.

When the supply voltage is lower than the working voltage of the displacement WSN, the displacement WSN stops working; once the supply voltage reaches the working voltage, the WSN immediately enters the activation state. The activation process is divided into three steps: startup, receiving and transmitting. The whole process of activation lasts about 5 s. The WSN can only be successfully activated and send data to the wireless gateway if the supply voltage is always within the working voltage range during the activation process.

5.2. Energy management circuit (EMC)

The storage capacitor consists of several mF-level electrolytic capacitors connected in parallel, as shown in Fig. 19. If this storage capacitor is used to directly power the WSN, when the capacitor voltage rises to the working voltage of the WSN, the WSN immediately enters the activation state and rapidly consumes energy, so that the capacitor voltage is rapidly reduced below the working voltage in the startup process, resulting in the WSN to stop working and activation fails. Therefore, it is necessary to introduce a suitable EMC between the storage capacitor and the WSN to control the charging and discharging of the storage capacitor. Moreover, at least two input voltage thresholds are required for the EMC so that the storage capacitor can continuously discharge between these two voltage thresholds and provide continuous power to the WSN during its activation process.

The AP64500 chip produced by the Diodes Incorporated is used in the EMC, as shown in Fig. 19. It is a 5 A, synchronous buck converter with a wide input voltage range of 3.8 V to 40 V. The AP64500

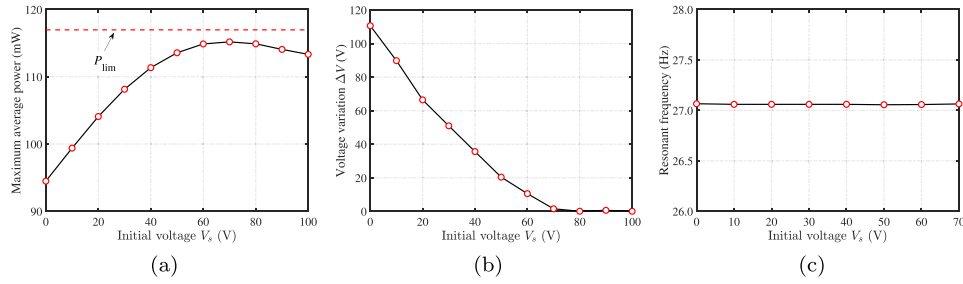


Fig. 17. Effect of the initial voltage across C_r on (a) the maximum average charging power of the D-M PEH, (b) voltage variation ΔV of the optimal C_r , and (c) the resonant frequency after one minute of charging duration.

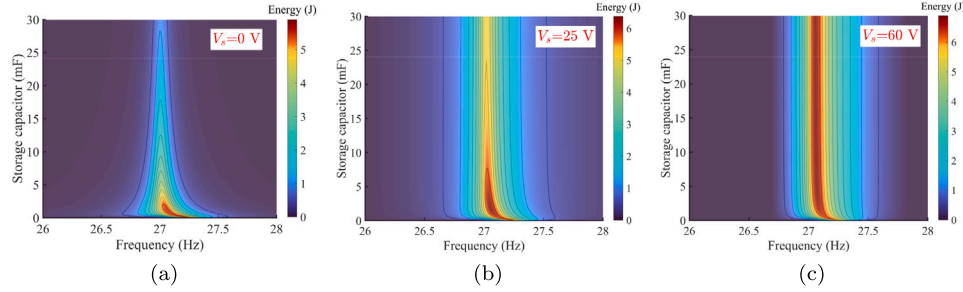


Fig. 18. Effect of capacitance of C_r and excitation frequency on the stored energy of C_r , with different initial voltages V_s after one minute of charging duration. ($A_0 = 0.359 \text{ m/s}^2$).

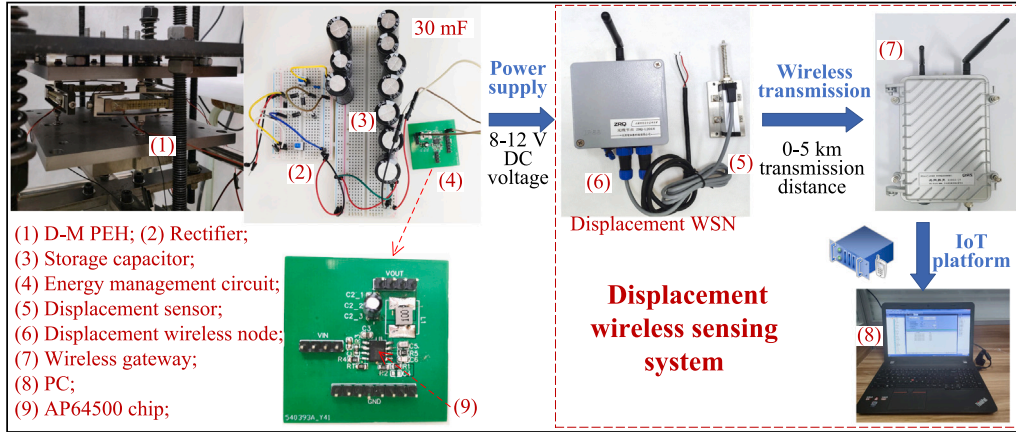


Fig. 19. Experiment layout of the activation test for the SP-WHMS.

chip fully integrates a 45 mΩ high-side power MOSFET and a 20 mΩ low-side power MOSFET to provide high-efficiency step-down DC-DC conversion. More details can be found and downloaded from the corresponding web page (<https://www.diodes.com/assets/Datasheets/AP64500.pdf>). Fig. 20(a) shows the layout of the EMC, which consists of an AP64500 chip and its peripheral circuit. The AP64500 chip has adjustable output voltages starting from 0.8 V using an external resistive divider R_1 , which can be determined by the following equation:

$$R_1 = R_2 \left(\frac{V_{OUT}}{0.8(V)} - 1 \right) \quad (9)$$

where R_2 is usually takes the value of 22 kΩ; V_{OUT} is the stabilized output voltage and is expected to be 9 V to meet the working voltage of the WSN. Substituting $V_{OUT} = 9 \text{ V}$ and $R_2 = 22 \text{ k}\Omega$ and into Eq. (9) yields $R_1 = 225.5 \text{ k}\Omega$. In this work, a resistor with a resistance of 220 kΩ is selected for R_1 , and the output voltage $V_{OUT} = 8.8 \text{ V}$. In addition, the AP64500 chip has an undervoltage lockout (UVLO) comparator that monitors the input voltage (VIN). Two external resistive dividers (R_3 and R_4) configures the VIN UVLO threshold voltages, as shown in

Fig. 20(b). The resistive divider resistor values are calculated by:

$$R_3 = \frac{0.924V_{ON} - V_{OFF}}{4.114(\mu\text{A})} \quad (10)$$

$$R_4 = \frac{1.09R_3}{V_{OFF} - 1.09(V) + 5.5(\mu\text{A})R_3} \quad (11)$$

where V_{ON} and V_{OFF} ($V_{ON} > V_{OFF}$) are the rising edge VIN voltage and the falling edge VIN voltage, respectively. The relationship between VIN and VOUT is shown in Fig. 21. When VIN is lower than V_{OFF} (state 1), the AP64500 chip disables, and $V_{OUT} \approx 0 \text{ V}$; When VIN rises above V_{ON} (state 3), the AP64500 chip works, and $V_{OUT} = 8.8 \text{ V}$; When VIN is between V_{OFF} and V_{ON} , if VIN is rising (state 2), the AP64500 chip disables, and $V_{OUT} \approx 0 \text{ V}$, if VIN is falling (state 4), the AP64500 chip works, and $V_{OUT} = 8.8 \text{ V}$. Connecting the storage capacitor to the VIN pin of the EMC, and its discharging and non-discharging conditions at different states of capacitor voltage V_r are shown in Fig. 21. When V_r is lower than V_{OFF} (state 1), the capacitor does not discharge; When V_r rises above V_{OFF} and is rising (state 2), the capacitor still does not discharge; As V_r further rises above V_{ON} (state

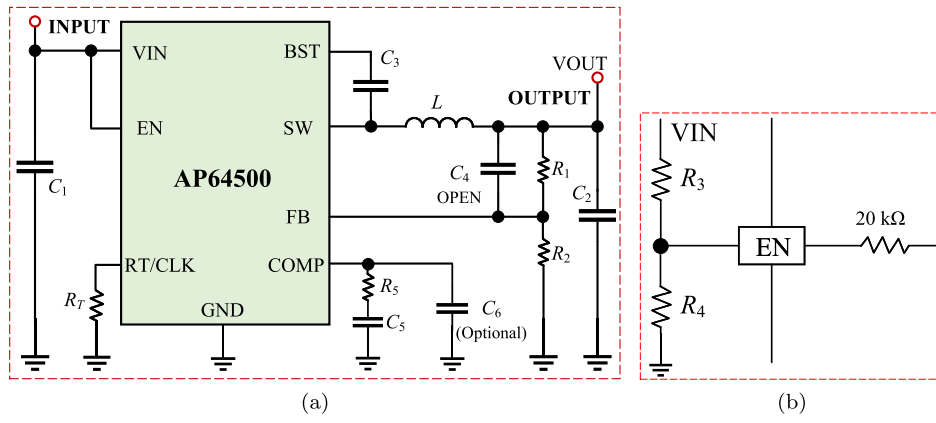


Fig. 20. (a) Layout of the energy management circuit and (b) programming UVLO.

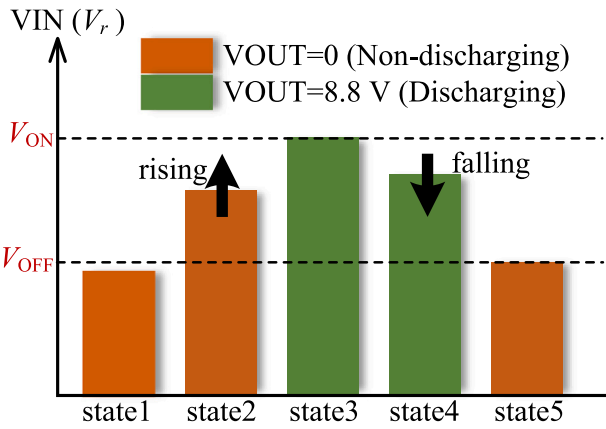


Fig. 21. The relation between V_{IN} and V_{OUT} of the AP64500 chip. (Discharging and non-discharging conditions of the storage capacitor at different states of V_r .)

3), the capacitor discharges until the V_r falls to V_{OFF} (state 5), and then the capacitor stops discharging again. The wide discharge voltage range between V_{ON} and V_{OFF} enables the storage capacitor to provide a stable and continuous power supply to the WSNs during the activation process of the WSNs.

5.3. Application

This part aims to test the effectiveness of the SP-WHMS being applied to the railway bridge through an activation experiment. The experiment layout is shown in Figs. 11 and 19, where the D-M PEH interfaces with the rectifier of the SEH circuit and a PC is used to receive the displacement data. The V_{IN} and V_{OUT} pins of the EMC are connected to the storage capacitor and the displacement WSN, respectively.

The steel base can approximately simulate the vibration of the real bridge by inputting the real acceleration time–history shown in Fig. 15(a) into the vibration controller. However, the vibration of the steel base is affected by the inertial force of the D-M PEH during vibration, while the inertial force is negligible for the real bridge. Therefore, when the D-M PEH is mounted on the steel base, it causes the vibration response of the steel base to differ from the input real bridge acceleration signal. As seen in Fig. 15(b), the bridge acceleration spectrum has several distinct and discrete peaks. And according to the voltage–frequency response shown in Fig. 4(a), when the D-M PEH is subjected to the bridge acceleration activation shown in Fig. 15, its voltage output is mainly affected by the frequency component (27.79 Hz) corresponding to the first peak, while the other frequency

components corresponding to other peaks have almost no effect on the voltage output. Therefore, in the next work, a harmonic acceleration excitation is used to approximate the real bridge acceleration excitation. The frequency of the harmonic acceleration excitation is 27 Hz, which is close to the main frequency (27.79 Hz) of the real bridge acceleration (see Fig. 15(b)) and is consistent with the short-circuit natural frequency of the fabricated D-M PEH. An acceleration sensor is placed on the steel base to monitor the acceleration amplitude of the steel base, which is controlled around 0.359 m/s^2 (corresponding to the first peak acceleration of the bridge acceleration spectrum shown in Fig. 15(b)) by adjusting the signal amplifier. In this experiment, this harmonic acceleration excitation was continuously applied to the D-M PEH.

As discussed in Section 4, increasing the initial voltage of the storage capacitor before charging by the PEH can effectively improve the charging efficiency, but the energy loss of the AP64500 increases with the voltage difference between V_{IN} and V_{OUT} . Therefore, in order to increase the charging efficiency and reduce the energy loss, V_{OFF} is set to 25 V. In addition, to prevent the input voltage V_{IN} from exceeding the upper limit of the AP64500’s working voltage (40 V), V_{ON} is set to 30 V. According to Eqs. (10) and (11), a 510 kΩ resistor is selected for R_3 and a 20 kΩ resistor is selected for R_4 in this work.

Assuming the charging duration is 60 s, the optimum capacitance of C_r for $V_s = 25 \text{ V}$ should be between 1.8 mF and 3.2 mF according to Fig. 16(a). However, according to Eq. (7), even if the capacitance of C_r is 3.2 mF, the stored energy is only 440 mJ when the voltage is increased from 25 V to 30 V, which is much lower than the activation energy of the WSN (about 2 J), so a larger capacitance is need for C_r . As seen in Fig. 18(b), for the storage capacitors with initial voltage of 25 V, the energy stored in the capacitor of 30 mF (4.93 J) can reach 88.8% of the maximum stored energy (5.55 J) when the excitation frequency is 27 Hz. Therefore, a 30 mF storage capacitor is used as the storage capacitor in the test.

Fig. 22(a) shows the variations of the voltage across the storage capacitor (V_r , also refers to V_{IN}) and the output voltage V_{OUT} (also refers to the input voltage of the WSN) during charging and power supply. The capacitor voltage was charged to 24 V using a battery before charging with the D-M PEH. When V_r rises to 25 V, the AP64500 chip disables because V_r is rising, and V_{OUT} is at low level. Since a small amount of charge remaining in the filter capacitor C_2 of the EMC, V_{OUT} is not zero. When V_r rises further to 30.19 V, the AP64500 chip works, the voltage of C_2 and V_{OUT} rise rapidly and remain at 8.8 V, and the WSN enters the activation state. During the activation process, which lasts about 5 s, V_r falls continuously and reaches 27.37 V at the end of activation process. Immediately after the activation process is complete, the WSN enters into the low-power standby state, meanwhile, V_r continues to rise, and the AP64500 disables again. After the AP64500 disables, V_{OUT} can still maintain around 8.8 V due to

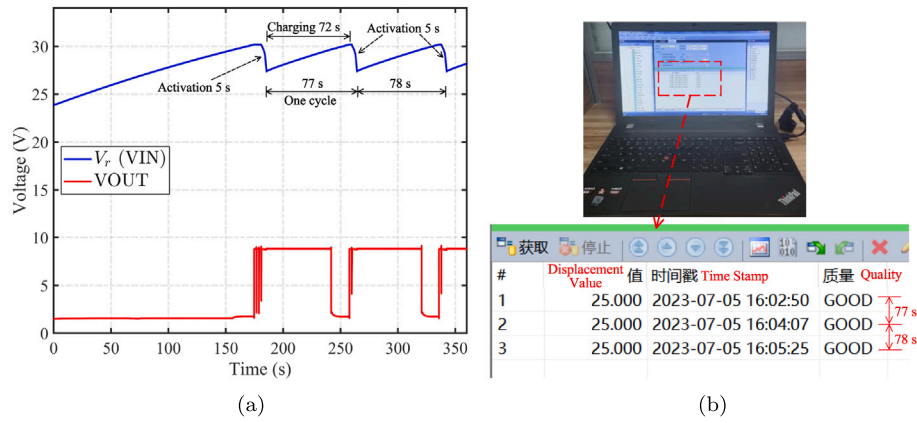


Fig. 22. (a) Variations of the voltage across the storage capacitor, V_r (VIN), and the output voltage, VOUT, with charging time in the activation testing; (b) Screenshot of displacement data received by the PC.

the presence of C_2 , so that the WSN does not stop working. After one data transmission cycle (60 s), the WSN enters the next activation state (at about 242 s in Fig. 22(a)), but at this time the AP64500 is still disabled because V_r is lower than V_{ON} (30.19 V), so the charge in C_2 is rapidly consumed by the WSN, causing the voltage across C_2 and VOUT rapidly drop to 1.75 V, and the WSN stops working. As V_r rises further and reaches 30.19 V, the WSN enters into the activation state again, and the above process begins again. The time interval between WSN activations is approximately 77 s, including approximate 72 s charging time and approximate 5 s activation time. The WSN was activated three times during the test. Correspondingly, the PC successfully received the displacement data every 77 s or so, and three sets of displacement data with good quality were received by the PC, as shown in Fig. 22(b). This means that the SP-WHMS can be successfully activated and normally operated under bridge vibration excitations, further demonstrates the feasibility of the SP-WHMS used on railway bridges. It should be noted that the reason why all displacement values are the same and equal to 25 is because the displacement sensor is completely stationary and not zeroed during the test.

The average charging power of the D-M PEH is approximately 33.75 mW. During the activation process of WSN (5 s), the energy in the storage capacitor is reduced by 2.435 J. Moreover, the D-M PEH is still vibrating and acting as a current source to continuously charge the capacitor, and the energy charged into the storage capacitor is approximately 0.169 J. Therefore, the total energy consumed by the WSN for a single data transmission is 2.6 J, which includes the energy loss of the energy management circuit.

Significantly, since the displacement WSN used in the experiment is based on LoRaWAN protocol, which has a long transmission distance and long activation time, the required energy of this WSN for a working cycle is relatively high, nearly 2 J in this work. However, for most of the WSNs based on Bluetooth protocol or ZigBee protocol, which have a short transmission distance and short activation time, the required activation energy in a working cycle is only in the mJ level [16,30,32]. Therefore, the proposed SP-WHMS is also useful for most of the WSNs based on the low-power Bluetooth protocol or ZigBee protocol.

5.4. Activation evaluation under real bridge acceleration excitation

The result of the activation test in section 5.3 shows that the SP-WHMS can be successfully activated and normally operated when the storage capacitor satisfies the following two conditions: (1) The voltage across the storage capacitor (V_r) reaches V_{ON} ; (2) The released energy of the storage capacitor exceeds the sum of the WSN activation energy and the EMC loss energy when V_r drops from V_{ON} to V_{OFF} . Therefore, we can determine whether the SP-WHMS is activated or not based on whether the storage capacitor satisfies the above two conditions during the

energy storage process. This part will investigate the activation status of the proposed SP-WHMS under real bridge acceleration excitations through numerical analysis and circuit simulation. The numerical results are calculated by the IAP, while the simulation results are obtained in SIMetrix, and the equivalent circuit is shown in Fig. 9.

The natural frequency of the D-M PEH is determined based on the train-induced vibration responses of the bridge, so before designing the D-M PEH, the vibration characteristics of the bridge need to be measured and analyzed first. In practical, the main factors affecting the vibration response of bridges are: the train type, the train running speed and track irregularity. When the dominant frequency of the bridge vibration varies due to these influence factors, it is needed to analyze the statistical distribution of the mechanical energy generated by the PEH subjected to bridge vibrations under operating conditions, and then use the optimization algorithm to determine the optimal resonance frequency of the PEH [50,51]. For some railway bridges, if these influence factors remain essentially constant, the dominant frequency of bridge vibration may also remain almost constant. In this part, we only intend to investigate the activation status of the SP-WHMS under the ideal acceleration excitations of the bridge, i.e., assuming that there is no change in the acceleration signals of the bridge induced by different train passages, and the acceleration signal is shown in Fig. 15. In order to maximize the energy storage efficiency, the mass of the fabricated D-M PEH was adjusted to 5.14 kg so that its short-circuited natural frequency (27.73 Hz) is slightly lower than the frequency (27.79 Hz) corresponding to the maximum peak of the frequency spectrum, as shown in Fig. 15(b).

First, the energy storage performance of the SP-WHMS is evaluated under multiple cyclic bridge acceleration excitations. Here, it should be pointed out that one cyclic bridge acceleration excitation means that the train runs one time on the bridge, and the time history of the one cycle acceleration excitation is shown in Fig. 15(a). For N_t cyclic bridge acceleration excitations, the train will run N_t times.

Fig. 23 shows the time histories of the voltage and energy variation of the storage capacitor, which has a capacitance of 20 mF and an initial voltage of 25 V, under one or multiple cyclic bridge acceleration excitations, where the energy variation of the storage capacitor is calculated by Eq. (7). Every rise in the curves means the D-M PEH is subjected to one cyclic bridge acceleration excitation. A sufficiently long free vibration duration was added after every cyclic excitation to ensure that the D-M PEH and bridge were stationary at the start of the next cyclic excitation. The difference between the circuit simulation results and IAP results is less than 1%, which proves that the IAP shown in Fig. 7 can accurately predict the charging process under non-harmonic excitations.

Increasing charging current is one of the most effective ways to improve the charging efficiency. Both series and parallel connections of

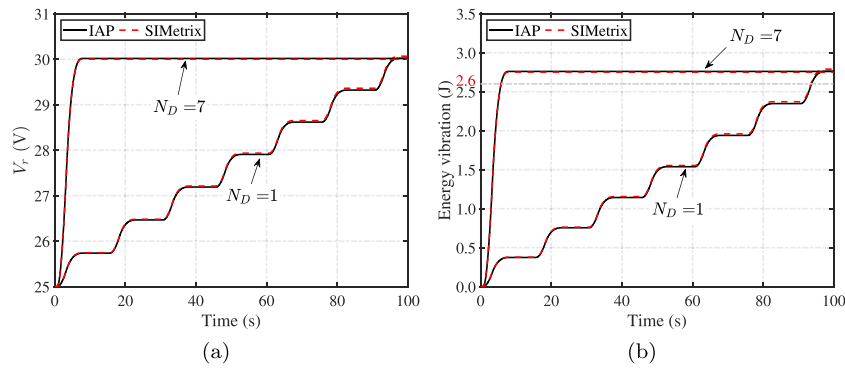


Fig. 23. Time histories of (a) the voltage and (b) energy variation of the storage capacitor under one or multiple cyclic bridge acceleration excitations. ($C_r = 20$ mF and $V_s = 25$ V; N_D denotes the number of the D-M PEHs.).

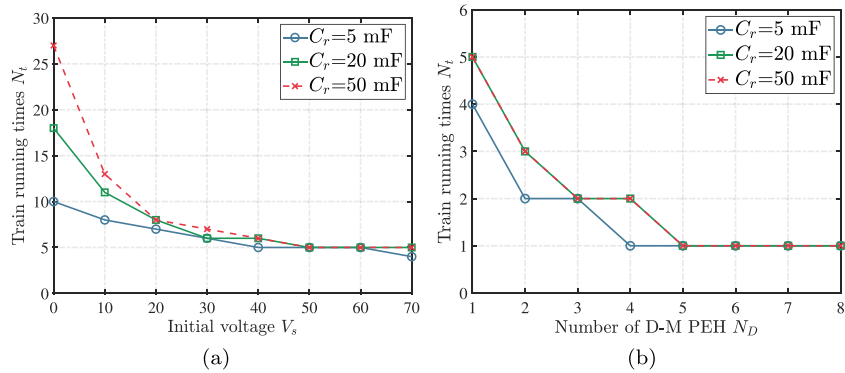


Fig. 24. The minimum train running times required to activate the WHMS under (a) different initial voltage V_s of the storage capacitor and (b) different number of D-M PEHs electricity contacted in parallel (where $V_s = 70$ V).

multiple PEHs can increase the energy charging efficiency, except that the former is done by increasing the output voltage while the latter is done by increasing the output current [15]. When the output voltage of a single PEH is difficult to meet the voltage demand, the output voltage can be increased by connecting multiple PEHs in series; When the output voltage of a single PEH meets the voltage demand, multiple PEHs can be connected in parallel to increase the output current. In this work, under the acceleration excitation of the bridge, the output open-circuit voltage of a single D-M PEH is much higher than the voltage thresholds V_{OFF} and V_{ON} of the energy management circuit, so increasing the charging current by connecting multiple D-M PEHs in parallel is more effective in improving the charging efficiency than increasing the voltage by connecting them in series. N_D in Fig. 23 denotes the number of the D-M PEHs used in the SP-WHMS. For the case of N_D D-M PEHs are electrically connected in parallel, the mass, the stiffness, the equivalent coupling coefficient and the equivalent capacitance are changed to $N_D m_p$, $N_D k_p$, $N_D \theta_p$ and $N_D C_p$, respectively [15]. A successful activation of the proposed SP-WHMS requires that the voltage on the storage capacitor exceeds 30 V and the stored energy exceeds 2.6 J. Here, the stored energy refers to the energy supplied by the D-M PEH, i.e., the total energy in the capacitor minus the initial energy. From Fig. 23, when only one D-M PEH is used, the train needs to run at least 7 times on the bridge to activate the SP-WHMS. In general, the average operation interval of each time for the Hada railway line is 5 min, so the wireless node in the SP-WHMS transmit data every 35 min. Using multiple D-M PEHs electrically connected in parallel to power the wireless node can effectively improve the charging efficiency. As seen in Fig. 23, at least 7 D-M PEHs are required if the SP-WHMS can be activated after the train has run only one time. However, too many D-M PEHs lead to a higher cost.

Assuming the energy management circuit has a higher upper limit of working voltage, the charging efficiency can be improved by increasing the initial voltage of the storage capacitor. Fig. 24(a) shows the

minimum train running times required to activate the SP-WHMS with one D-M PEH under different initial voltage of the storage capacitor. As the initial voltage of the storage capacitor increases toward V_{im} (nearly 70 V), the minimum train running times required decreases and then stabilizes. For a 5 mF storage capacitor with an initial voltage of 70 V, the train only needs to run four times to activate the SP-WHMS.

Furthermore, Fig. 24(b) shows the minimum train running times required to activate the SP-WHMS under different number of D-M PEHs electrically connected in parallel, where the initial voltages of all storage capacitors are 70 V. When 4 D-M PEHs and a 5 mF storage capacitor with an initial voltage of 70 V are used in the SP-WHMS, the train only needs to run one time to activate the SP-WHMS.

Finally, it should be noted that the above conclusions were drawn while ignoring the leakage of the storage capacitor. In practice, the storage capacitors may leak due to incomplete insulation of the internal medium, so in order to minimize leakage losses, the capacitor types with low leakage current should be preferred for storage capacitors.

6. Conclusion

An IoT-based SP-WHMS for a long-term and long-distance health monitoring of railway bridges is proposed and implemented in this work, in which a displacement WSN is used to monitor the displacement change of bridges. Moreover, the displacement WSN can also be used to monitor other bridge data that directly reflects the bridge health, such as crack width, slip and settlement. The whole-process of the SP-WHMS is analyzed from four parts: energy conversion, energy storage, energy management and application. A reported D-M PEH is refabricated and used to convert the bridge vibration energy into the electrical energy in the energy conversion process. In addition, some improved designs for increasing the charging efficiency of the SP-WHMS are also realized by comprehensively analyzing the effects

of some key factors in energy storage process, such as the excitation frequency, charging duration, capacitance of the storage capacitor, initial voltage of the storage capacitor, and number of the D-M PEH. Several major results and conclusions are summarized as follows.

- (1) The effectiveness of the SP-WHMS used on railway bridges is verified through a harmonic excitation experiment. In addition to the LoRaWAN-based displacement WSN tested in this work, the SP-WHMS is also useful for most of WSNs based on the low-power Bluetooth or ZigBee protocols. When the WSNs with long data transmission time or long activation time are used in the SP-WHMS, at least two input voltage thresholds are required for the energy management circuit so that the storage capacitor can continuously discharge between these two voltage thresholds and provide continuous power to the WSNs during their activation process.
- (2) A high-precision iteration analysis procedure (IAP) is proposed for predicting the charging process that a PEH interfaced with the SEH circuit under non-harmonic excitation. A comparison shows IAP's prediction deviates less than 3% from the experiment result and even less than 1% from the simulation result. Many existing theories on the charging process are based on the assumption of harmonic excitation and not applicable to the practical case of non-harmonic excitation, whereas the IAP does not have the limitation.
- (3) Under harmonic acceleration excitations, the maximum average charging power of the PEH interfaced with a SEH circuit cannot exceed the average power limit (P_{lim}) of the PEH connected to a pure resistor. Adjusting the short-circuit natural frequency of the D-M PEH slightly lower than the excitation frequency can effectively improve the charging efficiency. In addition, increasing the initial voltage of the storage capacitor appropriately before charging with the PEH can improve the charging power and enhance the robustness of the storage energy to the capacitance of the storage capacitor. For the fabricated D-M PEH in this work, under a harmonic acceleration excitation with the optimal frequency, when the initial voltage of the optimal storage capacitor reaches the circuit voltage amplitude (V_{lim}) corresponding to the average power limit (P_{lim}) of the D-M PEH connected to a pure resistor, the average charging power is maximum and up to 98.29% of P_{lim} .
- (4) Under harmonic acceleration excitations, the selection of suitable capacitance for the storage capacitor in a certain vibration environment should take into account the charging duration. The optimal capacitance of the storage capacitor to maximize the charging efficiency increase linearly with the charging duration, so when the optimal capacitance for a certain charging duration is known, the optimal capacitance for different charging durations can be predicted. This rule same goes for the maximum storage energy.
- (5) Generally, the charging efficiency of the SP-WHMS is proportional to the number of D-M PEHs connected in parallel. When the energy stored in the storage capacitor is not sufficient to activate the WSN after a train passes over the bridge, the times of the train runs on the bridge can be reduced by installing multiple D-M PEHs with the same resonance frequency in parallel on the bridge.

CRedit authorship contribution statement

Weiqiang Sheng: Writing – original draft, Validation, Methodology, Data curation, Conceptualization. **Hongjun Xiang:** Writing – review & editing, Supervision, Funding acquisition, Conceptualization. **Linglong Gao:** Methodology, Conceptualization. **Jianjun Wang:** Writing – review & editing, Supervision. **Junrui Liang:** Writing – review & editing, Supervision. **Zhiwei Zhang:** Writing – review & editing, Supervision.

Declaration of competing interest

The authors declare that they have no known competing financial interests or personal relationships that could have appeared to influence the work reported in this paper.

Data availability

Data will be made available on request.

Acknowledgments

This work is supported by the National Natural Science Foundation of China (Nos. 52078028 and 52108110) and Beijing Jiaotong University Education Foundation, China (No. 05060105). The authors also acknowledge Professor Jiawang Zhan and Graduate student Jintao Guo for their help.

Appendix. The expression of R_{opt}

$$R_{opt} = \frac{1}{\omega_0 C_p} \sqrt{\frac{(2v\xi_p)^2 + (1 - v^2)^2}{(2v\xi_p)^2 + (1 - v^2 + \kappa^2)^2}} \quad (A.1)$$

where v is the frequency ratio between the excitation frequency and the short-circuit D-M PEH, and is given by:

$$v = \sqrt{1 + \frac{\kappa^2}{2} - 2\xi_p^2 - \sqrt{\left(\frac{\kappa^2}{2} - 2\xi_p^2\right)^2 - 4\xi_p^2}} \quad (A.2)$$

References

- [1] Ahmad MM, Khan NM, Khan FU. Bridge vibration energy harvesting for wireless IoT-based structural health monitoring systems: A review. *J Intell Mater Syst Struct* 2023;34(19):2209–39.
- [2] Popovic N, Feltrin G, Jalsan KE, Wojtera M. Event-driven strain cycle monitoring of railway bridges using a wireless sensor network with sentinel nodes. *Struct Control Health Monit* 2017;24(7):e1934.
- [3] Ataei S, Nouri M, Kazemiashtiani V. Long-term monitoring of relative displacements at the keystone of a masonry arch bridge. *Struct Control Health Monit* 2018;25(4):e2144.
- [4] Magalhães F, Cunha Á, Caetano E. Vibration based structural health monitoring of an arch bridge: From automated OMA to damage detection. *Mech Syst Signal Process* 2012;28:212–28.
- [5] Mesquita E, Arêde A, Pinto N, Antunes P, Varum H. Long-term monitoring of a damaged historic structure using a wireless sensor network. *Eng Struct* 2018;161:108–17.
- [6] Salehi H, Burgueño R, Chakrabarty S, Lajnef N, Alavi AH. A comprehensive review of self-powered sensors in civil infrastructure: State-of-the-art and future research trends. *Eng Struct* 2021;234:111963.
- [7] Hou WQ, Li Yk, Guo W, Li JL, Chen YH, Duan XX. Railway vehicle induced vibration energy harvesting and saving of rail transit segmental prefabricated and assembling bridges. *J Cleaner Prod* 2018;182:946–59.
- [8] Hou WQ, Li YK, Zheng Y, Guo W. Multi-frequency energy harvesting method for vehicle induced vibration of rail transit continuous rigid bridges. *J Cleaner Prod* 2020;254:119981.
- [9] Cahill P, Nuallain NAN, Jackson N, Mathewson A, Karoumi R, Pakrashi V. Energy harvesting from train-induced response in bridges. *Abbreviation Title J Bridge Eng* 2014;19(9):04014034.
- [10] Zhang ZW, Xiang HJ, Shi ZF. Mechanism exploration of piezoelectric energy harvesting from vibration in beams subjected to moving harmonic loads. *Compos Struct* 2017;179:368–76.
- [11] Zhang YR, Xiang HJ, Deng HS, Zhang XB, Zhan JW, Shi ZF. System-level modeling and design method of an array of piezoelectric energy harvesters under typical ambient vibration. *J Intell Mater Syst Struct* 2023;34(3):261–78.
- [12] Wu N, Bao B, Wang Q. Review on engineering structural designs for efficient piezoelectric energy harvesting to obtain high power output. *Eng Struct* 2021;235:112068.
- [13] Zhang ZW, Xiang HJ, Shi ZF, Zhan JW. Experimental investigation on piezoelectric energy harvesting from vehicle-bridge coupling vibration. *Energy Convers Manage* 2018;163:169–79.

- [14] Hou WQ, Zheng Y, Guo W, Guo PC. Piezoelectric vibration energy harvesting for rail transit bridge with steel-spring floating slab track system. *J Cleaner Prod* 2021;291:125283.
- [15] Sheng WQ, Xiang HJ, Zhang ZW, Yuan XP. High-efficiency piezoelectric energy harvester for vehicle-induced bridge vibrations: Theory and experiment. *Compos Struct* 2022;299:116040.
- [16] Khan FU. Review of non-resonant vibration based energy harvesters for wireless sensor nodes. *J Renew Sustain Energy* 2016;8(4):044702.
- [17] Zhang XT, Zhang ZT, Pan HY, Salman W, Yuan YP, Liu YJ. A portable high-efficiency electromagnetic energy harvesting system using supercapacitors for renewable energy applications in railroads. *Energy Convers Manage* 2016;118:287–94.
- [18] Yang F, Gao MY, Wang P, Zuo JY, Dai J, Cong JL. Efficient piezoelectric harvester for random broadband vibration of rail. *Energy* 2021;218:119559.
- [19] Pan Y, Liu FW, Jiang RJ, Tu ZW, Zuo L. Modeling and onboard test of an electromagnetic energy harvester for railway cars. *Appl Energy* 2019;250:568–81.
- [20] Tao JX, Viet NV, Carpinteri A, Wang Q. Energy harvesting from wind by a piezoelectric harvester. *Eng Struct* 2017;133:74–80.
- [21] Iqbal M, Khan FU. Hybrid vibration and wind energy harvesting using combined piezoelectric and electromagnetic conversion for bridge health monitoring applications. *Energy Convers Manage* 2018;172:611–8.
- [22] Wang JY, Xiang HJ. Stochastic analysis of galloping piezoelectric energy harvesters under turbulent flow conditions based on the probability density evolution method. *Mech Syst Signal Process* 2023;200:110638.
- [23] Shu YC, Lien IC. Analysis of power output for piezoelectric energy harvesting systems. *Smart Mater Struct* 2006;15:1499–512.
- [24] Wang M, Yin PL, Li ZJ, Sun Y, Ding JH, Luo J, et al. Harnessing energy from spring suspension systems with a compressive-mode high-power-density piezoelectric transducer. *Energy Convers Manage* 2020;220:113050.
- [25] Zhang Z, Xiang H, Tang L. Modeling, analysis and comparison of four charging interface circuits for piezoelectric energy harvesting. *Mech Syst Signal Process* 2021;152:107476.
- [26] Schoeftner J, Buchberger G. A contribution on the optimal design of a vibrating cantilever in a power harvesting application-optimization of piezoelectric layer distributions in combination with advanced harvesting circuits. *Eng Struct* 2013;53:92–101.
- [27] Tabesh A, Fréchet LG. A low-power stand-alone adaptive circuit for harvesting energy from a piezoelectric micropower generator. *IEEE Trans Ind Electron* 2009;57(3):840–9.
- [28] Zhang ZW, Xiang HJ, Tang LH, Yang WQ. A comprehensive analysis of piezoelectric energy harvesting from bridge vibrations. *J Phys D: Appl Phys* 2023;55(1):014001.
- [29] Sudhawiyangkul T, Isarakorn D. Design and realization of an energy autonomous wireless sensor system for ball screw fault diagnosis. *Sensors Actuators A* 2017;258:49–58.
- [30] Wang L, Luo G, Jiang Z, Zhang F, Maeda R. Broadband vibration energy harvesting for wireless sensor node power supply in train container. *Rev Sci Instrum* 2019;90(12):125003.
- [31] Han Y, Wu F, Du XZ, Li ZH, Chen HX, Guo DX, et al. Enhance vortices vibration with Y-type bluff body to decrease arousing wind speed and extend range for flag triboelectric energy harvester. *Nano Energy* 2024;109063.
- [32] Wang JJ, Cao YL, Xiang HJ, Zhang ZW, Liang JR, Li X, et al. A piezoelectric smart backing ring for high-performance power generation subject to train induced steel-spring fulcrum forces. *Energy Convers Manage* 2022;257:115442.
- [33] Hu GB, Zhao CY, Yang YW, Li X, Liang JR. Triboelectric energy harvesting using an origami-inspired structure. *Appl Energy* 2022;306:118037.
- [34] Li X, Teng L, Tang H, Chen JY, Wang HY, Liu Y, et al. ViPSN: A vibration-powered IoT platform. *IEEE Internet Things J* 8(3):1728–39.
- [35] Zhou QH, Zheng K, Hou L, Xing JY, Xu RT. Design and implementation of open LoRa for IoT. *IEEE Access* 2019;7:100649–57.
- [36] Zhang B, Zhou HX, Zhao XL, Gao J, Zhou SX. Design and experimental analysis of a piezoelectric energy harvester based on stacked piezoceramic for nonharmonic excitations. *Energy* 2023;282:128948.
- [37] Guyomar D, Badel A, Lefeuvre E, Richard C. Toward energy harvesting using active materials and conversion improvement by nonlinear processing. *IEEE Trans Ultrason Ferroelectr Freq Control* 2005;52(4):584–95.
- [38] Ottman GK, Hofmann HF, Bhatt AC, Lesieutre GA. Adaptive piezoelectric energy harvesting circuit for wireless remote power supply. *IEEE Trans Power Electron* 2002;17(5):669–76.
- [39] Lefeuvre E, Badel A, Richard C, Guyomar D. Piezoelectric energy harvesting device optimization by synchronous electric charge extraction. *J Intell Mater Syst Struct* 2005;16(10):865–76.
- [40] Badel A, Guyomar D, Lefeuvre E, Richard C. Piezoelectric energy harvesting using a synchronized switch technique. *J Intell Mater Syst Struct* 2006;17:831–9.
- [41] Lefeuvre E, Badel A, Richard C, Petit L, Guyomar D. A comparison between several vibration-powered piezoelectric generators for standalone systems. *Sens Actuat A-Phys* 2006;126(2):405–16.
- [42] Lallart M, Garbuio L, Petit L, Richard C, Guyomar D. Double synchronized switch harvesting (DSSH): A new energy harvesting scheme for efficient energy extraction. *IEEE Trans Ultrason Ferroelectr Freq Control* 2008;55(10):2119–30.
- [43] Liao Y, Liang J. Maximum power, optimal load, and impedance analysis of piezoelectric vibration energy harvesters. *Smart Mater Struct* 2018;27:075053.
- [44] Tang L, Yang Y. Analysis of synchronized charge extraction for piezoelectric energy harvesting. *Smart Mater Struct* 2011;20(8):085022.
- [45] Wu PH, Shu YC. Finite element modeling of electrically rectified piezoelectric energy harvesters. *Smart Mater Struct* 2015;24:094008.
- [46] Yang Y, Tang L. Equivalent circuit modeling of piezoelectric energy harvesters. *J Intell Mater Syst Struct* 2009;20:2223–35.
- [47] Saroufim A, Issa MA, Mahdi M, Issa MA. Proof load testing and shear assessment of Kishwaukee I-39-river bridge using the modified compression field theory. *J Civ Struct Health Monit* 2023;13(2):827–66.
- [48] Shi LH, Feng CB, Zhang TG, Sha SD, Su YW, Du SW, et al. Deformation monitoring of railway bridge group influenced by construction of metro tunnel. *Appl Mech Mater* 2013;405:1810–4.
- [49] Xiang W, Wei JY, Zhang FL. Structural health monitoring design and performance evaluation of a middle-span bridge. *Sensors* 2023;23(21):8702.
- [50] Peralta-Braz P, Alamdari MM, Ruiz RO, Atroschenko E, Hassan M. Design optimisation of piezoelectric energy harvesters for bridge infrastructure. *Mech Syst Signal Process* 2023;205:110823.
- [51] Cámara-Molina JC, Romero A, Moliner E, Connolly DP, Martínez-Rodrigo MD, Yurchenko D, et al. Design, tuning and in-field validation of energy harvesters for railway bridges. *Mech Syst Signal Process* 2024;208:111012.